

Theory of Subcycle Linear Momentum Transfer in Strong-Field Tunneling Ionization

Hongcheng Ni,^{1,2,*} Simon Brennecke,³ Xiang Gao,² Pei-Lun He,^{4,†} Stefan Donsa,² Iva Březinová,² Feng He,⁴ Jian Wu,¹ Manfred Lein,³ Xiao-Min Tong,⁵ and Joachim Burgdörfer^{2,‡}

¹*State Key Laboratory of Precision Spectroscopy, East China Normal University, Shanghai 200241, China*

²*Institute for Theoretical Physics, Vienna University of Technology, 1040 Vienna, Austria, EU*

³*Institut für Theoretische Physik, Leibniz Universität Hannover, 30167 Hannover, Germany, EU*

⁴*Key Laboratory for Laser Plasmas (Ministry of Education) and School of Physics and Astronomy, Collaborative Innovation Center for IFSA (CICIFSA), Shanghai Jiao Tong University, Shanghai 200240, China*

⁵*Center for Computational Sciences, University of Tsukuba, Tsukuba, Ibaraki 305-8573, Japan*

Interaction of a strong laser pulse with matter transfers not only energy but also linear momentum of the photons. Recent experimental advances have made it possible to detect the small amount of linear momentum delivered to the photoelectrons in strong-field ionization of atoms. We present numerical simulations as well as an analytical description of the subcycle phase (or time) resolved momentum transfer to an atom accessible by an attoclock protocol. We show that the light-field-induced momentum transfer is remarkably sensitive to properties of the ultrashort laser pulse such as its carrier-envelope phase and ellipticity. Moreover, we show that the subcycle resolved linear momentum transfer can provide novel insight into the interplay between nonadiabatic and nondipole effects in strong-field ionization. This work paves the way towards the investigation of the so-far unexplored time-resolved nondipole nonadiabatic tunneling dynamics.

Strong-field ionization is typically well described in the dipole approximation, in which the vector potential \mathbf{A} of the electromagnetic field as well as the electric field \mathbf{F} are assumed to be homogeneous while the magnetic field vanishes. Consequently, also the Poynting vector and the classical radiation pressure vanish. Thus, the strong field does not transfer linear momentum to the atomic target. The dipole approximation is usually well justified for typical laser parameters employed in strong-field ionization, i.e., in the socalled dipole oasis [1]. Remarkably, nondipole effects can be enhanced along two rather different routes: either by reducing the laser wavelength such that it approaches the atomic scale thereby probing the inhomogeneity of the electromagnetic field. This gives rise to photoionization with an angular distribution deviating from the dipole shape [2–5]. Alternatively, nondipole effects can also be enhanced by increasing the laser wavelength and/or increasing the intensity so that the motion of the liberated electron is strongly influenced by the magnetic field and the radiation pressure of the laser field [6–12].

Due to the photon dispersion relation $p = \mathcal{E}/c$ (c : the speed of light), the momentum of a single photon in the propagation direction imparted on the target, p_z , is very small and is usually overshadowed by the transverse momentum $p_{\perp} \sim \sqrt{2\mathcal{E}}$ gained by the departing electron from the photon energy \mathcal{E} , while other photon properties such as angular momentum [13–15] or helicity [16–18] have much more easily observable effects. With recent advances in detecting technologies, the small momentum shift p_z in the laser propagation direction has become observable. In 2011, Smeenk *et al.* studied experimentally the sharing of the absorbed photon momentum between the photoelectron and the residual ion in tunneling ionization [6]. The photon momentum transfer could be viewed as a two-step process [9]. In the first step of under-barrier tunneling, the electron and ion move together as a composite system, thus the ion gains almost all the photon momentum I_p/c since it is much heavier than the electron (I_p : the ioniza-

tion potential). In the second step of continuum motion, the liberated electron gains the momentum E/c , where E is the final electron energy.

Further theoretical studies [19–21] found that the photon momentum transferred in the tunneling step is not given entirely to the ion due to the action of the laser magnetic field during the tunneling dynamics, resulting in the estimate for the final linear momentum of the ionized electron in the laser propagation direction

$$\langle p_z \rangle = E/c + \beta I_p/c, \quad (1)$$

where β denotes the fraction of the momentum transferred to the electron during the tunneling step. Estimates for the ground-state hydrogen atom vary between $\beta = 0.3$ [19, 20] and $\beta = 1/3$ [20, 21].

While most previous studies focused on the momentum transfer by the entire ultrashort pulse, very recently the first transverse-momentum-resolved study [9, 10] and angle-resolved measurement of $\langle p_z \rangle$ [11] using an attoclock setup [22, 23] became available. We present in the following the first ab-initio quantum simulation of the subcycle linear momentum transfer of the electron in strong-field ionization resolved in time. We refer to this process as light-field-induced momentum transfer since effects of quantization of the radiation field, i.e., photonic properties, play no significant role in the strong-field regime. The cycle-averaged light-field momentum transfer is closely related to the classical radiation pressure. We show that the subcycle resolved momentum transfer $\langle p_z(\phi_p) \rangle$ (ϕ_p is the attoclock angle in the polarization plane, Fig. 1) sensitively depends on the optical properties of the ultrashort pulse, most notably its carrier-envelope phase (CEP) and polarization. Conceptually importantly, it provides novel insights into the momentum sharing between the departing electron and the residual ion. By employing the backpropagation method [24–26], we are able to separate the longitudinal momentum transferred during the tunneling pro-

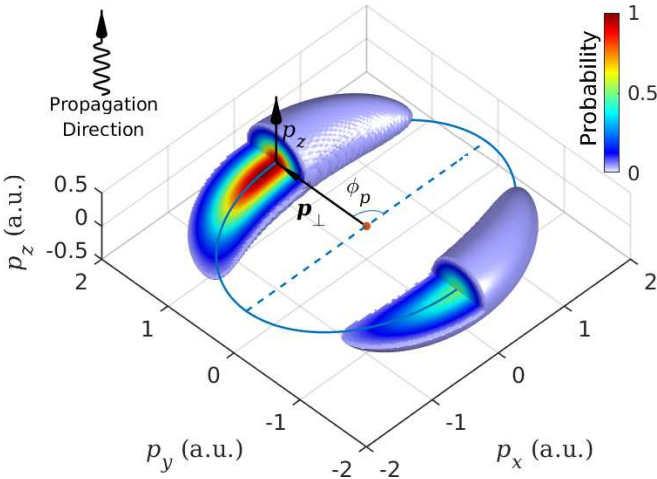


FIG. 1. Attoclock protocol for subcycle resolved electron emission with momentum $\mathbf{p} = (p_{\perp}, p_z)$ with the longitudinal component p_z along the propagation direction and the transverse component p_{\perp} in the polarization plane. For a few-cycle pulse with ellipticity ϵ , the classical cycle-averaged radiation pressure picture suggests $\langle p_z \rangle > 0$.

cess and during the continuum motion of the liberated electron on a subcycle scale. We identify modulations stemming from the nonadiabatic tunneling dynamics demonstrating an interplay between the nonadiabatic and nondipole tunneling effects.

We numerically solve the time-dependent Schrödinger equation (TDSE) for strong-field ionization of helium with the single-active-electron approximation beyond the dipole approximation by including all corrections to first order in the fine-structure constant $1/c$ (in atomic units). The corresponding Hamiltonian is given by [9, 27]

$$H = \frac{1}{2} \left[\mathbf{p} + \mathbf{A}(t) + \frac{e_z}{c} \left(\mathbf{p} \cdot \mathbf{A}(t) + \frac{1}{2} \mathbf{A}^2(t) \right) \right]^2 + V \left(\mathbf{r} - \frac{z}{c} \mathbf{A}(t) \right), \quad (2)$$

where the (x, y) plane is the laser polarization plane (denoted by the subscript \perp) and \hat{z} is along the direction of the laser propagation and longitudinal momentum transfer (Fig. 1), \mathbf{p} is the momentum operator, \mathbf{r} is the position operator, $V(\mathbf{r})$ is the effective potential for the helium atom [28], and $\mathbf{A}(t) = \mathbf{A}(t, z = 0)$ is the laser vector potential at the position of the nucleus. In the following, we choose $\mathbf{A}(t) = A_0 \cos^4(\frac{\omega t}{2N}) [\sin(\omega t + \phi_{\text{CEP}}) \mathbf{e}_x - \epsilon \cos(\omega t + \phi_{\text{CEP}}) \mathbf{e}_y]$, where A_0 is the peak amplitude along the major axis, ϵ is the ellipticity, ω is the central angular frequency, N is the total number of cycles, and ϕ_{CEP} is the CEP. The corresponding electric field is defined as $\mathbf{F}(t) = -\dot{\mathbf{A}}(t)$. We use a laser pulse with a wavelength of $\lambda = 800$ nm, a total intensity of 5×10^{14} W/cm², a total number of cycles $N = 6$, an ellipticity $\epsilon = 0.75$, and $\phi_{\text{CEP}} = 0$ or $\pi/2$, unless specified otherwise. For these laser parameters, the Keldysh parameter amounts to 0.80, corresponding to ionization in the near tunneling regime. Since a short laser pulse is used, the ponderomotive gradient from the

laser focus does not transfer any net linear momentum to the electron [6]. We note that nondipole effects will increase in the midinfrared with λ^2 (see [29]). We demonstrate here that they are already observable in the near-infrared. The TDSE is solved by two alternative methods to check for convergence. We use the split-operator Fourier method on a grid with 1024 points in each dimension, a grid step of 0.35 a.u., and a time step of 0.03 a.u. The simulation box is separated smoothly into an inner part and an outer part by an absorbing boundary of the form $1/[1 + \exp\{(r - r_0)/d\}]$, where $r_0 = 164$ a.u. and $d = 4$ a.u. The inner part is propagated using the full Hamiltonian and the outer part using a Coulomb-free Hamiltonian. At each time step, the absorbed wave function is projected onto the nondipole Volkov solution [20, 30] to incrementally obtain the momentum distribution [31, 32]. In addition, to initialize the backpropagation method, we place a sphere of 6000 evenly distributed virtual detectors [33–36] at a radius $r_{\text{vd}} = 40$ a.u. to convert the quantum flux into an ensemble of classical trajectories [29], which are subsequently propagated backward in time to retrieve the tunneling exit characteristics [17, 24–26]. r_{vd} is chosen such that no unphysical intercycle interference distorts the backpropagation thereby protecting the phase gradient as the local momentum [33, 34]. We have checked that the results do not depend on the particular choice of r_{vd} and are converged with respect to the number of virtual detectors used. The electronic wave function is propagated for an additional cycle period after the conclusion of the laser pulse such that most ionized electronic flux reached the detector sphere. Alternatively, the TDSE is also solved with the generalized pseudospectral method [37–39], where the time propagation of the nondipole contribution is treated using a Taylor expansion in combination with a split-operator method [29]. We have verified that the two numerical methods give virtually identical results.

In order to explore analytically the partitioning of the light-field-induced momentum transfer between electron and ion in tunneling ionization in the subcycle regime, we have extended the strong-field approximation (SFA) to include both nondipole and nonadiabatic effects simultaneously (ndSFA). Accordingly, after applying the stationary phase approximation, the tunneling ionization rate is given by [40–42]

$$W_{\text{ndSFA}} = |\tilde{S}|^{-\alpha_Z} \exp\{2\text{Im}S\}, \quad (3)$$

with $S = \int_{t_s}^{t_r} \left\{ \frac{1}{2} [\mathbf{p} + \mathbf{A}(t) + \frac{e_z}{c} (\mathbf{p} \cdot \mathbf{A}(t) + \frac{1}{2} \mathbf{A}^2(t))]^2 + I_p \right\} dt$ [20, 30] evaluated at the saddle-point time $t_s = t_r + it_i$ with $\alpha_Z = 1 + Z/\sqrt{2I_p}$ (Z is the asymptotic charge of the remaining ion). Eq. (3) includes nonadiabatic as well as nondipole effects and keeps track of nonexponential prefactors, thereby going beyond exponential accuracy. Remarkably, all of these factors leave their signature on the subcycle resolved longitudinal momentum transfer $\langle p_z \rangle$. The present ndSFA tunneling description allows to disentangle the longitudinal momentum transfer during tunneling from that of the free motion after tunneling with subcycle resolution.

The initial kinetic momentum at the tunnel exit \mathbf{v} is related to the final momentum \mathbf{p} by $\mathbf{v} = \mathbf{p} + \mathbf{A} + \frac{e_z}{c} [(\mathbf{p}_{\perp} + \mathbf{A})^2 -$

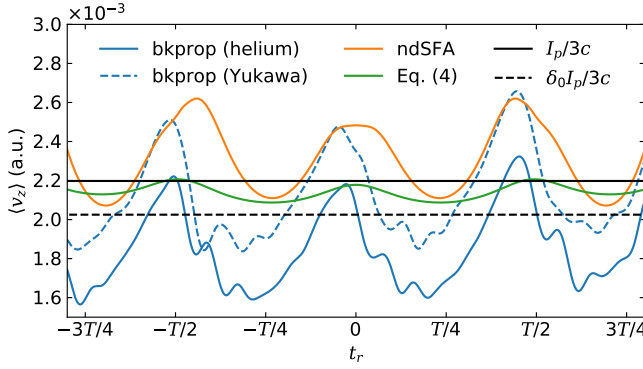


FIG. 2. Subcycle time-resolved linear momentum transfer at the tunnel exit for a sine-like pulse $\phi_{\text{CEP}} = \pi/2$. Blue curve: backpropagation of TDSE wave packet (bkprop) for the helium potential (solid curve) and the short-range Yukawa-like potential (dashed curve); orange curve: ndSFA using $\alpha_0 = 1$; green curve: analytical prediction for $\langle v_z \rangle$ [Eq. (4)] using $\alpha_0 = 1$; black solid curve: $I_p/3c$; black dashed curve: $\delta_0 I_p/3c$, with $\delta_0 = 1 - 2\alpha_0 F_0/(2I_p)^{3/2}$.

$p_\perp^2] = \mathbf{p} + \mathbf{A} + \frac{e_z}{2c} (v_\perp^2 - p_\perp^2)$. The ndSFA prediction for \mathbf{v} can be tested against the numerical results from the backpropagation of the full TDSE solution. The time-resolved longitudinal momentum at the tunnel exit $\langle v_z(t_r) \rangle$ is found to be approximately given by (see [29], Eq. (S29))

$$\langle v_z(t_r) \rangle = \frac{\tilde{I}_p(t_r)}{3c} \left[1 - \frac{2\alpha_Z F(t_r)}{(2I_p)^{3/2}} \right], \quad (4)$$

with an effective ionization potential $\tilde{I}_p(t_r) \equiv I_p + \langle v_\perp^2(t_r) \rangle/2$ accounting for the energy shift by the initial transverse tunneling momentum. Here, t_r is the tunneling exit time, the real part of the complex saddle-point time $t_s = t_r + it_i$. The correction term proportional to F approximately incorporates also the influence from the nonexponential prefactor. The asymptotic longitudinal momentum $\langle p_z(t_r) \rangle$ follows as [10, 29]

$$\langle p_z(t_r) \rangle = \Delta E/c + \langle v_z(t_r) \rangle. \quad (5)$$

Eq. (5) provides the subcycle decomposition of the light-field-induced longitudinal momentum transfer into one part associated with the tunneling dynamics $\langle v_z \rangle$ and another associated with the free-particle motion of the liberated electron with $\Delta E = \frac{1}{2}(\langle p_\perp^2 \rangle - \langle v_\perp^2 \rangle)$. For $\langle v_\perp^2 \rangle \ll \langle p_\perp^2 \rangle$ and $\alpha_Z = 0$, Eq. (5) resembles the cycle-averaged limit [Eq. (1)] previously discussed [19–21]. However, significant modifications appear. Only the energy gained in the streaking field after ionization, ΔE , rather than the total energy E , contributes to the first term [9, 10]. More importantly, the longitudinal momentum transfer during tunneling $\langle v_z(t_r) \rangle$ displays a 2ω subcycle oscillation and additionally a downward shift relative to the value $I_p/3c$ (Fig. 2). Scrutinizing Eq. (4), we can identify different contributions: neglecting $\langle v_\perp^2 \rangle$ and the pre-exponential prefactor ($\alpha_Z = 0$), Eq. (4) reduces to $\langle v_z \rangle = I_p/3c$ (black solid line). Including the prefactor for a short-range potential ($\alpha_0 = 1$), the t_r -independent part is shifted

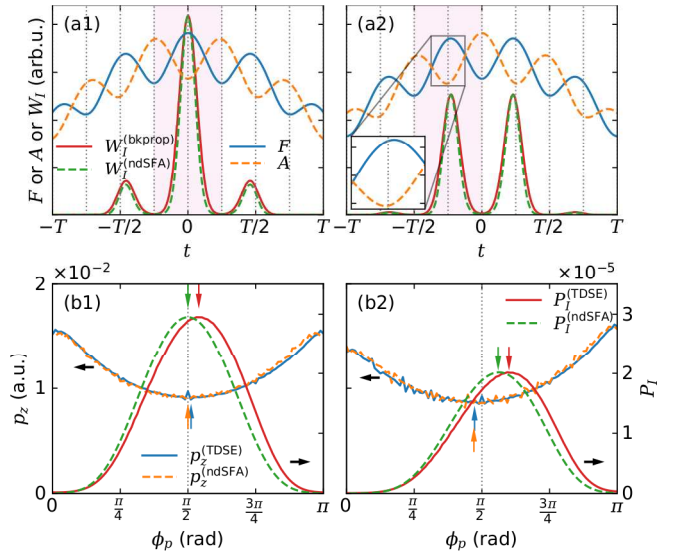


FIG. 3. Row (a): Absolute magnitude of the electric field $F(t)$ and vector potential $A(t)$ of the ultrashort few-cycle pulse with $\phi_{\text{CEP}} = 0$ (left column) and $\phi_{\text{CEP}} = \pi/2$ (right column). Also shown is the tunneling ionization rate $W_I(t = t_r)$ calculated by backpropagation of the TDSE solution (bkprop) and the ndSFA using $\alpha_1 = 1 + 1/\sqrt{2I_p}$ (see text) as a function of the tunneling exit time t_r . Row (b): Asymptotic longitudinal momentum transfer $\langle p_z(\phi_p) \rangle$ (left ordinate) and ionization probability $P_I(\phi_p)$ (right ordinate) as a function of the attoclock angle ϕ_p calculated by TDSE and ndSFA for the attoclock signal corresponding to the shaded temporal half cycle in row (a). The arrows mark the phases of the maxima of P_I and minima of $\langle p_z \rangle$.

downward to $\langle v_z \rangle = I_p/3c[1 - 2\alpha_0 F_0/(2I_p)^{3/2}]$ (black dashed line), with the prefactor evaluated at the field peak $F_0 = A_0\omega$ where the ionization probability maximizes. It approximately agrees with the minima for the backpropagated wave packet in a Yukawa-like potential $V(r) = -[1.17822 \exp(-0.2r) + \exp(-0.5r^2)]/\sqrt{r^2 + 0.14328}$ with the same I_p as helium (blue dashed curve). On top of this downward shift, nonadiabaticity contributes to an upward shift $\sim \langle v_\perp^2(t_r) \rangle$ featuring a 2ω subcycle oscillation reproduced by both Eq. (4) and the ndSFA. Finally, backpropagation from the full helium potential (blue solid curve) reveals an additional downward shift due to the presence of Coulomb attraction during the under-barrier motion of the ionizing electron.

The subcycle variation of the ionization probability as well as of the light-field-induced momentum transfer is found to strongly depend on the CEP of the pulse (Fig. 3) shown for a cosine-like pulse ($\phi_{\text{CEP}} = 0$, left column) and a sine-like pulse ($\phi_{\text{CEP}} = \pi/2$, right column). The tunneling ionization rates obtained by the ndSFA reproduce (up to a scaling factor) quite well the rates determined by the full quantum TDSE forward propagation followed by the semiclassical backward propagation [Fig. 3(a)]. While the cosine-like pulse yields a single dominant peak at the pulse center $t = 0$ (left column), the sine-like pulse gives rise to two peaks of comparable magnitude (right column). Note that for the few-cycle elliptic pulse, the phase shift between the peaks in the

$A(t)$ and the $F(t)$ fields deviates from $\pi/2$ and becomes itself time dependent [Fig. 3(a)]. Within the attoclock setting, the asymptotic momentum distribution projected onto the laser polarization plane provides information on the subcycle phase (or attoclock angle), $\phi_p = \arctan(p_y/p_x)$. This phase can be mapped onto the phase of the electromagnetic field through the attoclock (or streaking) principle $\mathbf{p}_\perp \approx -\mathbf{A}$ thereby allowing to extract subcycle timing information from the rotating \mathbf{A} field vector. The peak position of the ionization probability $P_I(\phi_p)$ is phase shifted between the full TDSE solution and the ndSFA [Fig. 3(b)] which is a well known signature of the Coulomb scattering of the outgoing electron neglected in the ndSFA. More surprisingly, the peak position of $P_I(\phi_p)$ varies strongly with ϕ_{CEP} [Fig. 3(b)]. In fact, this variation, virtually identical for both the TDSE and the ndSFA, is significantly larger than the Coulomb-field-induced shift. The momentum distribution $P(\phi_p, p_z)$ (Fig. 1) features a slight asymmetry in p_z representing a signature of nondipole effects. In most previous studies [6–8, 12, 19–21], the mean shift in p_z has been examined, i.e., $\langle p_z \rangle = \int d\phi_p dp_z p_z P(\phi_p, p_z) / \int d\phi_p dp_z P(\phi_p, p_z)$. We resolve the shift in p_z at a given attoclock angle, i.e., $\langle p_z(\phi_p) \rangle = \int dp_z p_z P(\phi_p, p_z) / \int dp_z P(\phi_p, p_z)$ [Fig. 3(b)]. The subcycle dependence of $\langle p_z(\phi_p) \rangle$, predicted by the full TDSE solution is well reproduced by the ndSFA [Eq. (3)] despite the fact that the ndSFA does not account for the Coulomb interaction of the outgoing electron with the residual ion. The Coulomb interaction is, thus, not important for the asymptotic longitudinal momentum transfer. This is due to the fact that, to leading order, Coulomb-laser coupling is absent as there is no laser field in the propagation direction. Of course, the Coulomb-induced momentum shift in the polarization plane would affect the momentum transfer in the propagation direction through the magnetic field, which is, however, a higher order effect and much smaller [10]. We note that, for linear polarization, the Coulomb effect plays a much more important role in the asymptotic longitudinal momentum transfer, both for single [7, 8] and double ionization [12].

For ellipticities well below $\epsilon = 1$, $\langle p_z \rangle$ features a pronounced minimum near $\phi_p \approx \pi/2$ (for details see [29]). This follows directly from Eq. (5). The energy imparted by the streaking field \mathbf{F} , is approximately given by $\Delta E = (\langle p_\perp^2 \rangle - \langle v_\perp^2 \rangle) / 2 \approx A^2 / 2$. Since the magnitude of the electric field $F(t)$ reaches its maximum near $\phi_p \approx \pi/2$, $A(t)$ reaches a local minimum at this angle which, in turn, translates into a minimum of $\langle p_z \rangle$. The precise position of this minimum $\phi_p(p_z^{\min})$ depends, however, sensitively on the CEP. While for a cosine-like pulse ($\phi_{\text{CEP}} = 0$), $\phi_p(p_z^{\min})$ is located at $\phi_p = \pi/2$, for a sine-like pulse ($\phi_{\text{CEP}} = \pi/2$), the minimum is shifted to smaller ϕ_p [Fig. 3(b)]. Also this variation can be understood as a consequence of Eq. (5): for $\phi_{\text{CEP}} = 0$, the maximum of F coincides with the minimum of A [Fig. 3(a1)]; for $\phi_{\text{CEP}} = \pi/2$, the maximum of F and the minimum of A are slightly displaced from each other from the expected instance of time at $\omega t = \pm\pi/2$ (inset Fig. 3(a2), see also [29]) which results in the observed phase shift. Such subcycle modulation of the

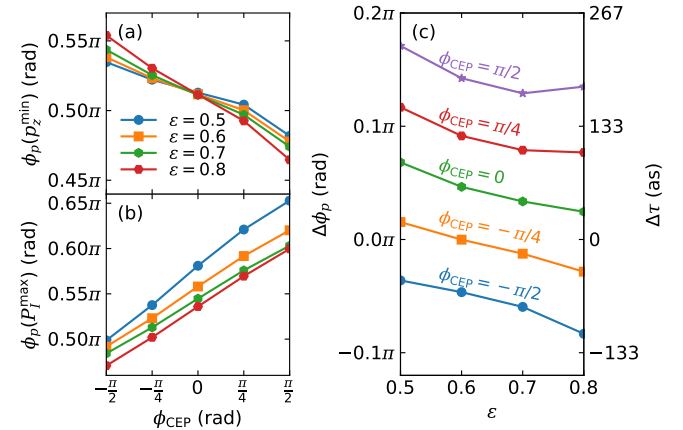


FIG. 4. The dependence of the attoclock angle $\phi_p(p_z^{\min})$ (a) and $\phi_p(p_z^{\max})$ (b) on the CEP for different ellipticities. The attoclock angle differences $\Delta\phi_p$ between $\phi_p(p_z^{\min})$ and $\phi_p(p_z^{\max})$ as a function of ellipticity ϵ for different CEP's (c) (left ordinate) can be converted to a time delay $\Delta\tau$ in attoseconds (right ordinate).

linear momentum transfer will survive focal volume averaging since the above observation is independent of the laser intensity.

Both the angle of the minimum of $\langle p_z(\phi_p) \rangle$, $\phi_p(p_z^{\min})$, and the angle of the maximum of $P_I(\phi_p)$, $\phi_p(p_z^{\max})$, feature a systematic variation as a function of the ellipticity and the CEP [Figs. 4(a) and 4(b)]. Here, we focus on the first attoclock ionization peaks $[0 < \phi_p < \pi]$, shaded area in Fig. 3(a)]. The value of $\phi_p(p_z^{\min})$ for a sine-like ($\phi_{\text{CEP}} = \pi/2$) and a (-1) sine-like pulse ($\phi_{\text{CEP}} = -\pi/2$) differ from each other [Fig. 4(a)]. The light-field-induced longitudinal momentum $\langle p_z(\phi_p) \rangle$ for an ultrashort pulse is a manifestly non-inversion-symmetric observable. In principle, the ϕ_{CEP} dependence of $\langle p_z \rangle$ could provide a novel protocol for the measurement of the CEP for ultrashort elliptically polarized pulses similar to the stereo-ATI [43] and the surface-electron emission protocol [44, 45] for linearly polarized pulses. The major difficulty in applying this idea is the smallness of the effect for near-infrared pulses. It could possibly be overcome for pulses in the midinfrared as $\langle p_z \rangle \sim \lambda^2$ (see [29]).

For elliptically polarized pulses, the phase shift $\Delta\phi_p$ between the minimum of $\langle p_z \rangle$ and the maximum of P_I , $\Delta\phi_p = \phi_p(p_z^{\max}) - \phi_p(p_z^{\min})$, can be directly converted into a time delay $\Delta\tau = \Delta\phi_p / \omega$ [Fig. 4(c)]. We find time delays of the order of tens of attoseconds. Such time delays have been indeed recently observed, however without control of the CEP [11]. In view of the strong CEP dependence revealed by our simulation [Fig. 4(c)], the interpretation of this delay has remained inconclusive. In turn, future CEP resolved measurements of $\Delta\tau$ would offer to probe the decomposition of the light-field-induced linear momentum transfer into the tunneling and continuum contributions [Eq. (5)] in unprecedented detail.

In summary, we have simulated the subcycle time-resolved light-field-induced transfer of linear momentum beyond dipole approximation during strong-field tunneling ionization

employing an attoclock protocol. A pronounced minimum in the momentum transfer is found along the minor axis of the polarization ellipse where the ionization probability peaks. The attoclock phase angle or timing of the minimum in the momentum transfer is shown to be strongly dependent on the carrier-envelope phase. By comparison between the back-propagation of the full TDSE solution to the tunnel exit and a novel strong-field approximation including nondipole and nonadiabatic effects, distinct contributions to the light-field-induced momentum transfer on a subcycle scale could be identified. The mean momentum shift is found to be sensitive to sub-exponential as well as Coulomb contributions to tunneling. Nonadiabatic corrections result in a 2ω subcycle modulation of the transferred momentum at the tunnel exit. This appears to be the first direct evidence of an interplay between nonadiabatic and nondipole tunneling effects. The longitudinal momentum transfer thus promises to offer new insights into the strong-field tunneling dynamics.

This work was supported by Project No. 11904103, 11774023, 11574205 of the National Natural Science Foundation of China (NSFC), Project No. M2692 and doctoral college W1243 of the Austrian Science Fund (FWF), the Programme Quantum Dynamics in Tailored Intense Fields (QUTIF) of the Deutsche Forschungsgemeinschaft (DFG), Project No. MA14-002 of the Vienna Science and Technology Fund (WWTF), Project No. 19JC1412200 of the Shanghai Science and Technology Commission, Project No. 2018YFA0404802 and 2018YFA0306303 of the National Key R&D Program of China, and Project No. JP16K05495 of the Grant-in-Aid for Scientific Research of the Japan Society for the Promotion of Science. Numerical simulations were in part performed on the Vienna Scientific Cluster.

* hcni@lps.ecnu.edu.cn
 † a225633@sjtu.edu.cn
 ‡ joachim.burgdoerfer@tuwien.ac.at

[1] H. R. Reiss, *J. Phys. B* **47**, 204006 (2014).
 [2] O. Hemmers, R. Guillemin, and D. W. Lindle, *Radiat. Phys. Chem.* **70**, 123 (2004).
 [3] B. Krässig, E. P. Kanter, S. H. Southworth, R. Guillemin, O. Hemmers, D. W. Lindle, R. Wehlitz, and N. L. S. Martin, *Phys. Rev. Lett.* **88**, 203002 (2002).
 [4] S. Grundmann, F. Trinter, A. W. Bray, S. Eckart, J. Rist, G. Kastirke, D. Metz, S. Klumpp, J. Viehaus, L. Ph. H. Schmidt, J. B. Williams, R. Dörner, T. Jahnke, M. S. Schöffler, and A. S. Kheifets, *Phys. Rev. Lett.* **121**, 173003 (2018).
 [5] S.-G. Chen, W.-C. Jiang, S. Grundmann, F. Trinter, M. S. Schöffler, T. Jahnke, R. Dörner, H. Liang, M.-X. Wang, L.-Y. Peng, and Q. Gong, *Phys. Rev. Lett.* **124**, 043201 (2020).
 [6] C. T. L. Smeenk, L. Arissian, B. Zhou, A. Mysyrowicz, D. M. Villeneuve, A. Staudte, and P. B. Corkum, *Phys. Rev. Lett.* **106**, 193002 (2011).
 [7] A. Ludwig, J. Maurer, B. W. Mayer, C. R. Phillips, L. Gallmann, and U. Keller, *Phys. Rev. Lett.* **113**, 243001 (2014).
 [8] N. Haram, I. Ivanov, H. Xu, K. T. Kim, A. Atia-tul-Noor, U. S. Sainadh, R. D. Glover, D. Chetty, I. V. Litvinyuk, and R. T. Sang, *Phys. Rev. Lett.* **123**, 093201 (2019).
 [9] A. Hartung, S. Eckart, S. Brennecke, J. Rist, D. Trabert, K. Fehre, M. Richter, H. Sann, S. Zeller, K. Henrichs, G. Kastirke, J. Hoehl, A. Kalinin, M. S. Schöffler, T. Jahnke, L. Ph. H. Schmidt, M. Lein, M. Kunitski, R. Dörner, *Nat. Phys.* **15**, 1222 (2019).
 [10] N. Eicke, S. Brennecke, and M. Lein, *Phys. Rev. Lett.* **124**, 043202 (2020).
 [11] B. Willenberg, J. Maurer, B. W. Mayer, and U. Keller, *Nat. Commun.* **10**, 5548 (2019).
 [12] F. Sun, X. Chen, W. Zhang, J. Qiang, H. Li, P. Lu, X. Gong, Q. Ji, K. Lin, H. Li, J. Tong, F. Chen, C. Ruiz, J. Wu, and F. He, *Phys. Rev. A* **101**, 021402(R) (2020).
 [13] F. Maulbetsch and J. Briggs, *J. Phys. B* **28**, 551 (1995).
 [14] H. Ni, S. Chen, C. Ruiz, and A. Becker, *J. Phys. B* **44**, 175601 (2011).
 [15] K. Henrichs, S. Eckart, A. Hartung, D. Trabert, J. Rist, H. Sann, M. Pitzer, M. Richter, H. Kang, M. S. Schöffler, M. Kunitski, T. Jahnke, and R. Dörner, *Phys. Rev. A* **97**, 031405(R) (2018).
 [16] I. Barth and O. Smirnova, *Phys. Rev. A* **84**, 063415 (2011).
 [17] K. Liu, H. Ni, K. Renziehausen, J. M. Rost, and I. Barth, *Phys. Rev. Lett.* **121**, 203201 (2018).
 [18] S. Eckart, M. Kunitski, M. Richter, A. Hartung, J. Rist, F. Trinter, K. Fehre, N. Schlott, K. Henrichs, L. Ph. H. Schmidt, T. Jahnke, M. Schöffler, K. Liu, I. Barth, J. Kaushal, F. Morales, M. Ivanov, O. Smirnova, and R. Dörner, *Nat. Phys.* **14**, 701 (2018).
 [19] S. Chelkowski, A. D. Bandrauk, and P. B. Corkum, *Phys. Rev. Lett.* **113**, 263005 (2014).
 [20] P.-L. He, D. Lao, and F. He, *Phys. Rev. Lett.* **118**, 163203 (2017).
 [21] M. Klaiber, E. Yakaboylu, H. Bauke, K. Z. Hatsagortsyan, and C. H. Keitel, *Phys. Rev. Lett.* **110**, 153004 (2013).
 [22] P. Eckle, M. Smolarski, P. Schlup, J. Biegert, A. Staudte, M. Schöffler, H. G. Müller, R. Dörner, and U. Keller, *Nat. Phys.* **4**, 565 (2008).
 [23] P. Eckle, A. N. Pfeiffer, C. Cirelli, A. Staudte, R. Dörner, H. G. Müller, M. Büttiker, and U. Keller, *Science* **322**, 1525 (2008).
 [24] H. Ni, U. Saalmann, and J. M. Rost, *Phys. Rev. Lett.* **117**, 023002 (2016).
 [25] H. Ni, U. Saalmann, and J. M. Rost, *Phys. Rev. A* **97**, 013426 (2018).
 [26] H. Ni, N. Eicke, C. Ruiz, J. Cai, F. Oppermann, N. I. Shvetsov-Shilovski, and L. W. Pi, *Phys. Rev. A* **98**, 013411 (2018).
 [27] S. Brennecke and M. Lein, *J. Phys. B* **51**, 094005 (2018).
 [28] X. M. Tong and C. D. Lin, *J. Phys. B* **38**, 2593 (2005).
 [29] Supplemental Material.
 [30] N. J. Kylstra, R. M. Potvliege, and C. J. Joachain, *J. Phys. B* **34**, L55 (2001).
 [31] M. Lein, E. K. U. Gross, and V. Engel, *Phys. Rev. Lett.* **85**, 4707 (2000).
 [32] X. M. Tong, K. Hino, and N. Toshima, *Phys. Rev. A* **74**, 031405(R) (2006).
 [33] B. Feuerstein and U. Thumm, *J. Phys. B* **36**, 707 (2003).
 [34] X. Wang, J. Tian, and J. H. Eberly, *Phys. Rev. Lett.* **110**, 243001 (2013).
 [35] J. P. Wang and F. He, *Phys. Rev. A* **95**, 043420 (2017).
 [36] Q. Zhang, G. Basnayake, A. Winney, Y. F. Lin, D. Debrah, S. K. Lee, and W. Li, *Phys. Rev. A* **96**, 023422 (2017).
 [37] X. M. Tong and S.-I. Chu, *Chem. Phys.* **217**, 119 (1997).
 [38] X. M. Tong, *J. Phys. B* **50**, 144004 (2017).
 [39] X. Gao and X. M. Tong, *Phys. Rev. A* **100**, 063424 (2019).
 [40] G. F. Gribakin and M. Y. Kuchiev, *Phys. Rev. A* **55**, 3760 (1997).

- [41] T. K. Kjeldsen and L. B. Madsen, Phys. Rev. A **74**, 023407 (2006).
- [42] D. B. Milošević, G. G. Paulus, D. Bauer, and W. Becker, J. Phys. B **39**, R203 (2006).
- [43] G. G. Paulus, F. Grasbon, H. Walther, P. Villoresi, M. Nisoli, S. Stagira, E. Priori, and S. De Silvestri, Nature **414**, 182 (2001).
- [44] Ch. Lemell, X.-M. Tong, F. Krausz, and J. Burgdörfer, Phys. Rev. Lett. **90**, 076403 (2003).
- [45] A. Apolonski, P. Domki, G. G. Paulus, M. Kakehata, R. Holzwarth, Th. Udem, Ch. Lemell, K. Torizuka, J. Burgdörfer, T. W. Hänsch, and F. Krausz, Phys. Rev. Lett. **92**, 073902 (2004).

Supplemental Material: Theory of Subcycle Linear Momentum Transfer in Strong-Field Tunneling Ionization

Hongcheng Ni,^{1,2} Simon Brennecke,³ Xiang Gao,² Pei-Lun He,⁴ Stefan Donsa,² Iva Březinová,² Feng He,⁴ Jian Wu,¹ Manfred Lein,³ Xiao-Min Tong,⁵ and Joachim Burgdörfer²

¹*State Key Laboratory of Precision Spectroscopy, East China Normal University, Shanghai 200241, China*

²*Institute for Theoretical Physics, Vienna University of Technology, 1040 Vienna, Austria, EU*

³*Institut für Theoretische Physik, Leibniz Universität Hannover, 30167 Hannover, Germany, EU*

⁴*Key Laboratory for Laser Plasmas (Ministry of Education) and School of Physics and Astronomy, Collaborative Innovation Center for IFSA (CICIFSA), Shanghai Jiao Tong University, Shanghai 200240, China*

⁵*Center for Computational Sciences, University of Tsukuba, Tsukuba, Ibaraki 305-8573, Japan*

S1. BACKPROPAGATION IN THE NONDIPOLE REGIME

In order to extract accurate information on the momentum distribution of ionized electrons at the tunnel exit, we extend the backpropagation method [1–3] to the nondipole regime. The method involves two steps: We first propagate the quantum wave packet forward in time until an ensemble of virtual detectors is reached. In the second step, semiclassical trajectories are propagated backward in time until the tunnel exit is reached. To initiate the backpropagation, the outgoing flux needs to be converted into classical trajectories when the laser field is still on. To this end, we need to find the appropriate flux associated with the Hamiltonian. The time-dependent Schrödinger equation can be written as

$$i\frac{\partial}{\partial t}\psi = \left\{ \frac{1}{2} \left[\mathbf{p} + \mathbf{A}(t) + \frac{e_z}{c} \left(\mathbf{p} \cdot \mathbf{A}(t) + \frac{1}{2} A^2(t) \right) \right]^2 + V \left(\mathbf{r} - \frac{z}{c} \mathbf{A}(t) \right) \right\} \psi, \quad (\text{S1})$$

the conjugate of which is

$$-i\frac{\partial}{\partial t}\psi^* = \left\{ \frac{1}{2} \left[-\mathbf{p} + \mathbf{A}(t) + \frac{e_z}{c} \left(-\mathbf{p} \cdot \mathbf{A}(t) + \frac{1}{2} A^2(t) \right) \right]^2 + V \left(\mathbf{r} - \frac{z}{c} \mathbf{A}(t) \right) \right\} \psi^*. \quad (\text{S2})$$

Multiplying Eq. (S1) by ψ^* from the left, multiplying Eq. (S2) by ψ from the left, and doing the subtraction, we have

$$\begin{aligned} i\frac{\partial}{\partial t}|\psi|^2 &= \frac{1}{2}\psi^* \left[\mathbf{p} + \mathbf{A}(t) + \frac{e_z}{c} \left(\mathbf{p} \cdot \mathbf{A}(t) + \frac{1}{2} A^2(t) \right) \right]^2 \psi - \frac{1}{2}\psi \left[-\mathbf{p} + \mathbf{A}(t) + \frac{e_z}{c} \left(-\mathbf{p} \cdot \mathbf{A}(t) + \frac{1}{2} A^2(t) \right) \right]^2 \psi^* \\ &= -i\nabla \cdot \left\{ \frac{1}{2}(\psi^* \mathbf{p} \psi - \psi \mathbf{p} \psi^*) + \mathbf{A} \left[|\psi|^2 + \frac{1}{2c}(\psi^* p_z \psi - \psi p_z \psi^*) + \frac{1}{2c^2}(\psi^* \mathbf{p} \cdot \mathbf{A} \psi - \psi \mathbf{p} \cdot \mathbf{A} \psi^*) + \frac{A^2}{2c^2}|\psi|^2 \right] \right. \\ &\quad \left. + \frac{e_z}{2c}(\psi^* \mathbf{p} \cdot \mathbf{A} \psi - \psi \mathbf{p} \cdot \mathbf{A} \psi^*) + \frac{e_z}{2c}A^2|\psi|^2 \right\}. \end{aligned} \quad (\text{S3})$$

According to the equation of continuity $\frac{\partial}{\partial t}\rho + \nabla \cdot \mathbf{j} = 0$, where $\rho \equiv |\psi|^2$, the probability flux \mathbf{j} is given by

$$\begin{aligned} \mathbf{j} &= \frac{1}{2}(\psi^* \mathbf{p} \psi - \psi \mathbf{p} \psi^*) + \mathbf{A} \left[|\psi|^2 + \frac{1}{2c}(\psi^* p_z \psi - \psi p_z \psi^*) + \frac{1}{2c^2}(\psi^* \mathbf{p} \cdot \mathbf{A} \psi - \psi \mathbf{p} \cdot \mathbf{A} \psi^*) + \frac{A^2}{2c^2}|\psi|^2 \right] \\ &\quad + \frac{e_z}{2c}(\psi^* \mathbf{p} \cdot \mathbf{A} \psi - \psi \mathbf{p} \cdot \mathbf{A} \psi^*) + \frac{e_z}{2c}A^2|\psi|^2. \end{aligned} \quad (\text{S4})$$

If we write the wavefunction in “polar” form as $\psi = \sqrt{\rho}e^{iS}$, we find

$$\mathbf{j} = \rho \nabla S + \rho \mathbf{A} \left\{ 1 + \frac{1}{c} \left[\frac{\partial S}{\partial z} + \frac{1}{c} \left(\nabla S \cdot \mathbf{A} + \frac{1}{2} A^2 \right) \right] \right\} + \rho \frac{e_z}{c} \left(\nabla S \cdot \mathbf{A} + \frac{1}{2} A^2 \right). \quad (\text{S5})$$

Expressing the current density as $\mathbf{j} = \rho \mathbf{v}$, we obtain the local velocity \mathbf{v} during the pulse

$$\mathbf{v} = \nabla S + \mathbf{A} \left\{ 1 + \frac{1}{c} \left[\frac{\partial S}{\partial z} + \frac{1}{c} \left(\nabla S \cdot \mathbf{A} + \frac{1}{2} A^2 \right) \right] \right\} + \frac{e_z}{c} \left(\nabla S \cdot \mathbf{A} + \frac{1}{2} A^2 \right). \quad (\text{S6})$$

Note that the Hamiltonian we use adds a “shear” to the atomic potential, effectively changing the velocity defined in this frame as compared to the lab frame. In order to obtain the observables in the lab frame, the following frame transform is required:

$$\mathbf{r}_{\text{lab}} = \mathbf{r} - z \mathbf{A} / c, \quad (\text{S7})$$

$$\mathbf{v}_{\text{lab}} = \mathbf{v} + z \mathbf{F} / c - v_z \mathbf{A} / c. \quad (\text{S8})$$

S2. THE GENERALIZED PSEUDOSPECTRAL METHOD FOR NONDIPOLE THREE-DIMENSIONAL TDSE

The Hamiltonian used in the main text [Eq. (2)] is presented in a “sheared” gauge to facilitate TDSE simulations with the Fourier method. To check the numerical convergence of the Fourier method, we also developed the generalized pseudospectral method to solve the three-dimensional TDSE beyond the dipole approximation using a length-gauge Hamiltonian with nondipole corrections to order $1/c$:

$$H_L = \left[\frac{1}{2} \tilde{\mathbf{p}}^2 + V(r) \right] + \mathbf{r} \cdot \mathbf{F}(t) + \frac{z}{c} \tilde{\mathbf{p}} \cdot \mathbf{F}(t) = H_0 + H_1 + H_2, \quad (\text{S9})$$

with $H_0 = \tilde{\mathbf{p}}^2/2 + V(r)$, $H_1 = \mathbf{r} \cdot \mathbf{F}(t)$, and $H_2 = \frac{z}{c} \tilde{\mathbf{p}} \cdot \mathbf{F}(t)$, where $\tilde{\mathbf{p}}$ is the corresponding canonical momentum. The part $H_0 + H_1$ is the Hamiltonian in dipole approximation in length gauge, and can be readily solved by the time propagator based on the second-order split-operator method [4] and the generalized pseudospectral method [5–7]. With the use of a Taylor expansion for the time propagator of the H_2 term, we can perform numerical simulations with the Hamiltonian H_L in a similar framework. More specifically, the time propagator for H_L can be expressed as

$$U(t + \Delta t) = \exp(-iH_0\Delta t/2) \exp(-iH_1\Delta t/2) \exp(-iH_2\Delta t) \exp(-iH_1\Delta t/2) \exp(-iH_0\Delta t/2). \quad (\text{S10})$$

The propagation of $\exp(-iH_0\Delta t/2)$ is done in energy space, and $\exp(-iH_1\Delta t/2)$ is evaluated in position space. Afterwards, we continue evaluating the $\exp(-iH_2\Delta t)$ part in position space using a Taylor expansion

$$\exp(-iH_2\Delta t) \approx \sum_{n=0}^{n_{\max}} \frac{(-iH_2\Delta t)^n}{n!}. \quad (\text{S11})$$

For the system considered in the present work, we found $n_{\max} = 8$ for each time step is adequate to obtain converged results. The momentum distribution is obtained using the same technique as in [8], except that the Volkov propagator applied to the absorbed wave packet at each time step is substituted with the nondipole version, which is calculated numerically with a similar procedure.

S3. NONDIPOLE STRONG-FIELD APPROXIMATION

The nondipole strong-field approximation (SFA) offers the possibility to model recollision-free strong-field ionization without the computational demanding solution of the exact time-dependent Schrödinger equation. For the calculations, we use the Hamiltonian in length gauge, H_L [Eq. (S9)], neglecting, however, the atomic potential in H_0 ,

$$H_L = \frac{1}{2} \tilde{\mathbf{p}}^2 + \mathbf{r} \cdot \mathbf{F}(t) + \frac{z}{c} \tilde{\mathbf{p}} \cdot \mathbf{F}(t). \quad (\text{S12})$$

The initial kinetic momentum (or velocity in a.u.) at the tunnel exit \mathbf{v} relates to the asymptotic momentum \mathbf{p} as

$$\mathbf{v} = \mathbf{p} + \mathbf{A} + \frac{e_z}{2c} [(\mathbf{p} + \mathbf{A})^2 - p^2] = \mathbf{p} + \mathbf{A} + \frac{e_z}{2c} (v_{\perp}^2 - p_{\perp}^2). \quad (\text{S13})$$

In the modified SFA evaluated in the saddle-point approximation, the transition rate is calculated from [9–11]

$$W_{\text{ndSFA}} = |\dot{S}|^{-\alpha_Z} \exp\{2\text{Im}S\}, \quad (\text{S14})$$

where $\alpha_Z = 1 + Z/\sqrt{2I_p}$ with Z the asymptotic charge of the remaining ion. For a short-range potential, $\alpha_Z = \alpha_0 = 1$. In the nondipole version of SFA (ndSFA), the action including nondipole corrections to the order $1/c$ can be expressed as [12]

$$S = \int_{t_s}^{t_r} \left\{ \frac{1}{2} \left[\mathbf{p} + \mathbf{A}(t) + \frac{e_z}{c} \left(\mathbf{p} \cdot \mathbf{A}(t) + \frac{1}{2} A^2(t) \right) \right]^2 + I_p \right\} dt. \quad (\text{S15})$$

The saddle point is given by

$$\frac{1}{2} \left[\mathbf{p} + \mathbf{A}(t_s) + \frac{e_z}{c} \left(\mathbf{p} \cdot \mathbf{A}(t_s) + \frac{1}{2} A^2(t_s) \right) \right]^2 + I_p = 0, \quad (\text{S16})$$

where the saddle-point time $t_s = t_r + it_i$ must be complex in order to solve Eq. (S16). After solving the saddle-point equation (S16) the photoelectron momentum distribution can be calculated directly by evaluating Eq. (S14). Reduced quantities such

as the ionization probability P_I as a function of the attoclock angle ϕ_p , as shown in Fig. 3(b) of the main text, follow from integration over the remaining variables. However, in order to calculate observables as a function of the release time t_r we have to integrate over all momenta that belong to this given real part of the saddle-point time. To this end, it is advantageous to perform a coordinate transformation $(p_x, p_y, p_z) \rightarrow (t_r, k_{\perp}, p_z)$ with the release time t_r chosen as the real part of the saddle-point time t_s , the momentum component in the polarization plane

$$k_{\perp} = (\mathbf{p} + \text{Re} \mathbf{A}(t_s)) \cdot (\text{Im} \mathbf{A}_y(t_s) \mathbf{e}_x - \text{Im} \mathbf{A}_x(t_s) \mathbf{e}_y) / \sqrt{(\text{Im} \mathbf{A}_x(t_s))^2 + (\text{Im} \mathbf{A}_y(t_s))^2} \quad (\text{S17})$$

and the z -component of the final momentum p_z . The probability density in these variables is accordingly given by

$$\tilde{w}(t_r, k_{\perp}, p_z) = \left| \det \frac{\partial(p_x, p_y, p_z)}{\partial(t_r, k_{\perp}, p_z)} \right| W_{\text{ndSFA}}(\mathbf{p}). \quad (\text{S18})$$

The subcycle time-resolved linear momentum transfer shown in Fig. 2 of the main text can now be obtained as the average of the initial velocity in the light propagation direction

$$\langle v_z(t_r) \rangle = \frac{\int dk_{\perp} dp_z v_z(t_r, k_{\perp}, p_z) \tilde{w}(t_r, k_{\perp}, p_z)}{\int dk_{\perp} dp_z \tilde{w}(t_r, k_{\perp}, p_z)}. \quad (\text{S19})$$

Expansion of the vector potential $\mathbf{A}(t_r + it_i)$ in powers of t_i [3, 13–16],

$$\mathbf{A}(t_r + it_i) = \mathbf{A}(t_r) - it_i \mathbf{F}(t_r) + \frac{1}{2} t_i^2 \dot{\mathbf{F}}(t_r) + O(t_i^3), \quad (\text{S20})$$

allows to simplify the ndSFA and to gain additional insights. Inserting into Eq. (S16) and keeping the terms up to the second order in t_i results in

$$\mathbf{v}(t_r) \cdot \mathbf{F}(t_r) = 0, \quad (\text{S21})$$

which is the termination criterion we use for the backpropagating trajectories, and

$$t_i = \sqrt{\frac{p^2 + (1 + \frac{p_z}{c}) [2\mathbf{p} \cdot \mathbf{A}(t_r) + A^2(t_r)] + 2I_p}{(1 + \frac{p_z}{c}) [F^2(t_r) - \mathbf{v}(t_r) \cdot \dot{\mathbf{F}}(t_r)]}}. \quad (\text{S22})$$

The ionization rate [Eq. (S14)] depends exponentially on the argument

$$\begin{aligned} \text{Im}S &= -I_p t_i - \frac{1}{2} \text{Re} \int_0^{t_i} \left[\mathbf{p} + \mathbf{A}(t_r + it) + \frac{\mathbf{e}_z}{c} \left(\mathbf{p} \cdot \mathbf{A}(t_r + it) + \frac{1}{2} A^2(t_r + it) \right) \right]^2 dt \\ &\approx - \frac{[p^2 + (1 + \frac{p_z}{c}) (2\mathbf{p} \cdot \mathbf{A}(t_r) + A^2(t_r)) + 2I_p]^{3/2}}{3 \sqrt{(1 + \frac{p_z}{c}) \tilde{F}(t_r)}}, \end{aligned} \quad (\text{S23})$$

with an effective field $\tilde{F}(t_r) = \sqrt{F^2(t_r) - \mathbf{v}_{\perp}(t_r) \cdot \dot{\mathbf{F}}(t_r)}$ and on the nonexponential prefactor

$$\begin{aligned} |\ddot{S}|^{-\alpha_Z} &\approx |-i(1 + p_z/c)t_i \tilde{F}^2|^{-\alpha_Z} \\ &\approx \left[\left(1 + \frac{p_z}{c} \right) \left(v_{\perp}^2 + p_z^2 + 2\frac{p_z}{c} \left(\mathbf{p} \cdot \mathbf{A} + \frac{A^2}{2} \right) + 2I_p \right) \tilde{F}^2 \right]^{-\alpha_Z/2}. \end{aligned} \quad (\text{S24})$$

Eq. (S23) can be further simplified

$$\begin{aligned} \text{Im}S &\approx - \frac{[v_{\perp}^2 + p_z^2 + \frac{p_z}{c} (v_{\perp}^2 - p_{\perp}^2) + 2I_p]^{3/2}}{3 \sqrt{(1 + \frac{p_z}{c}) \tilde{F}}} \\ &\approx - \frac{\left\{ \left(1 - \frac{p_z}{3c} \right) [v_{\perp}^2 + p_z^2 + \frac{p_z}{c} (v_{\perp}^2 - p_{\perp}^2) + 2I_p] \right\}^{3/2}}{3 \tilde{F}} \\ &\approx - \frac{1}{3 \tilde{F}} \left[v_{\perp}^2 + \left(p_z - \left(\frac{p_{\perp}^2 - v_{\perp}^2}{2c} + \frac{2I_p + v_{\perp}^2}{6c} \right) \right)^2 + 2I_p \right]^{3/2}, \end{aligned} \quad (\text{S25})$$

while Eq. (S24) can be accordingly approximated by

$$|\ddot{S}|^{-\alpha_Z} \approx \left[(v_{\perp}^2 + 2I_p) \tilde{F}^2 \right]^{-\alpha_Z/2} \left(1 + \frac{p_z}{c} \right)^{-\alpha_Z/2} \left[1 + \frac{p_z^2 + 2\frac{p_z}{c} \left(\mathbf{p} \cdot \mathbf{A} + \frac{A^2}{2} \right)}{v_{\perp}^2 + 2I_p} \right]^{-\alpha_Z/2} \\ \approx \left[(v_{\perp}^2 + 2I_p) \tilde{F}^2 \right]^{-\alpha_Z/2} \exp \left\{ -\frac{\alpha_Z}{2} \frac{p_z}{c} \right\} \exp \left\{ -\frac{\alpha_Z}{2} \frac{\left(p_z - \frac{p_{\perp}^2 - v_{\perp}^2}{2c} \right)^2}{v_{\perp}^2 + 2I_p} \right\}. \quad (\text{S26})$$

Hence, we arrive at

$$W_{\text{ndSFA}} \approx \left[(v_{\perp}^2 + 2I_p) \tilde{F}^2 \right]^{-\alpha_Z/2} \exp \left\{ -\frac{\alpha_Z}{2} \frac{p_z}{c} - \frac{\alpha_Z}{2} \frac{\left(p_z - \frac{p_{\perp}^2 - v_{\perp}^2}{2c} \right)^2}{v_{\perp}^2 + 2I_p} - \frac{2}{3\tilde{F}} \left[v_{\perp}^2 + \left(p_z - \left(\frac{p_{\perp}^2 - v_{\perp}^2}{2c} + \frac{2I_p + v_{\perp}^2}{6c} \right) \right)^2 + 2I_p \right]^{3/2} \right\} \\ \approx \left[(v_{\perp}^2 + 2I_p) \tilde{F}^2 \right]^{-\alpha_Z/2} \exp \left\{ -\frac{2}{3\tilde{F}} \left[v_{\perp}^2 + \left(1 + \frac{\alpha_Z \tilde{F}}{2(v_{\perp}^2 + 2I_p)^{3/2}} \right) \left(p_z - \left(\frac{p_{\perp}^2 - v_{\perp}^2}{2c} + \langle v_z(t_r, v_{\perp}) \rangle \right) \right)^2 + 2I_p \right]^{3/2} \right\}. \quad (\text{S27})$$

The Jacobian in Eq. (S18) reads after the expansion of the vector potential in t_i (S20)

$$\left| \det \frac{\partial(p_x, p_y, p_z)}{\partial(t_r, k_{\perp}, p_z)} \right| \approx \left| \frac{v_{\perp} \left[F_x(t_r) F'_y(t_r) - F'_x(t_r) F_y(t_r) \right]}{F^2(t_r)} + F(t_r) \right|. \quad (\text{S28})$$

To this order, it does not depend on p_z and, thus, has no influence in the transfer of longitudinal momentum. We therefore neglect this factor in the following.

In Eq. (S27), we introduce the partial average $\langle v_z(t_r, v_{\perp}) \rangle$ that is obtained by integration over p_z for fixed release time t_r and the perpendicular component of the velocity v_{\perp}

$$\langle v_z(t_r, v_{\perp}) \rangle = \frac{2I_p + v_{\perp}^2}{6c} \left[1 - \frac{2\alpha_Z \tilde{F}}{(2I_p + v_{\perp}^2)^{3/2}} \right] \approx \frac{2I_p + v_{\perp}^2}{6c} \left[1 - \frac{2\alpha_Z F}{(2I_p)^{3/2}} \right], \quad (\text{S29})$$

with the corresponding asymptotic linear momentum

$$\langle p_z(t_r, v_{\perp}) \rangle = \frac{p_{\perp}^2 - v_{\perp}^2}{2c} + \langle v_z(t_r, v_{\perp}) \rangle. \quad (\text{S30})$$

When focusing on the temporal dynamics only, one can additionally average over the perpendicular velocity v_{\perp} and hence obtain for a fixed release time t_r the average linear momentum transfer at the tunnel exit $\langle v_z(t_r) \rangle$.

The effective field $\tilde{F} = \sqrt{F^2 - \mathbf{v}_{\perp} \cdot \dot{\mathbf{F}}}$ including the time derivative of the field, $\dot{\mathbf{F}}$, accounts for nonadiabatic effects. Consequently, v_{\perp} is centered at nonzero values in Eqs. (S29) and (S30). Approximating the nonadiabatic correction to the lowest order in $\dot{\mathbf{F}}$ in the exponent

$$W_{\text{ndSFA}} \approx \left[(v_{\perp}^2 + 2I_p) \tilde{F}^2 \right]^{-\alpha_Z/2} \exp \left\{ -\frac{2}{3\tilde{F}} \left[(v_{\perp}^2 + 2I_p) \left(1 + \frac{\mathbf{v}_{\perp} \cdot \dot{\mathbf{F}}}{3F^2} \right) \right]^{3/2} \right\}, \quad (\text{S31})$$

where the first-order term in \mathbf{v}_{\perp} shifts the center of the v_{\perp} distribution from zero to a finite value. To obtain an explicit value, we have also neglected the momentum in the laser propagation direction, which would provide only a minimal contribution to the shift in v_{\perp} . Inserting the explicit expression for the laser field and assuming a flat envelope of the pulse yields

$$\langle v_{\perp}(t_r) \rangle \approx \frac{\epsilon I_p}{3A_0 \tilde{F}(t_r)^3} \quad \text{with} \quad \tilde{F}(t_r) = \sqrt{\cos^2(\omega t_r + \phi_{\text{CEP}}) + \epsilon^2 \sin^2(\omega t_r + \phi_{\text{CEP}})}, \quad (\text{S32})$$

which closely resembles the result of the Perelomov–Popov–Terent’ev (PPT) theory [17–23]. This nonadiabatic effect generates a subcycle modulation of the center of v_{\perp} as well as v_{\perp}^2 , which further results in a subcycle nonadiabatic modulation of the nondipole effect in Eq. (S31). If we approximate Eq. (S31) with a Gaussian distribution in v_{\perp} , it is easy to show that

$$\langle v_{\perp}^2(t_r) \rangle \approx \langle v_{\perp}(t_r) \rangle^2 + \frac{F(t_r)}{2\sqrt{2I_p}}. \quad (\text{S33})$$

Distinct contributions to the linear momentum at the tunnel exit [Eq. (S29)] can be studied at different levels of approximation. If we ignore the contribution from the nonexponential prefactor ($\alpha_Z = 0$),

$$\langle v_z(t_r) \rangle \approx \frac{2I_p + \langle v_{\perp}^2(t_r) \rangle}{6c} \approx \frac{I_p}{3c} + \frac{\varepsilon^2 I_p^2}{54c A_0^2 \hat{F}^6(t_r)} + \frac{F_0 \hat{F}(t_r)}{12c \sqrt{2I_p}}. \quad (\text{S34})$$

For $\varepsilon \lesssim 1$ as in a typical attoclock setup, Eq. (S34) can be further approximated by

$$\langle v_z \rangle \approx \frac{I_p}{3c} + \frac{1}{12c} \left[\frac{\varepsilon^2 I_p^2}{9A_0^2} (1 - \varepsilon^{-6}) + \frac{F_0}{2\sqrt{2I_p}} (1 - \varepsilon) \right] \cos(2\omega t_r + 2\phi_{\text{CEP}}) + \frac{1}{12c} \left[\frac{\varepsilon^2 I_p^2}{9A_0^2} (1 + \varepsilon^{-6}) + \frac{F_0}{2\sqrt{2I_p}} (1 + \varepsilon) \right]. \quad (\text{S35})$$

Obviously, the nonadiabaticity of strong-field tunneling ionization introduces a 2ω subcycle modulation of the nondipole transfer of photon momentum at the tunnel exit, in agreement with what is found in the main text. Note that for the present laser parameters $\frac{\varepsilon^2 I_p^2}{9A_0^2} (1 - \varepsilon^{-6}) + \frac{F_0}{2\sqrt{2I_p}} (1 - \varepsilon) < 0$, hence the modulation phase agrees with that presented in the main text as well. The temporal average of $\langle v_z(t_r) \rangle$, however, is larger than $I_p/3c$. The inclusion of the prefactor with $\alpha_Z > 0$ generates the downward shift in qualitative agreement with the results determined by the backpropagation method (black dashed line in Fig. 2 of the main text).

S4. ELLIPTICITY DEPENDENCE OF $\langle p_z \rangle$

The longitudinal momentum transfer $\langle p_z(\phi_p) \rangle$ features a characteristic dependence on the attoclock angle ϕ_p . However, the exact quantity is strongly dependent on the ellipticity of the ultrashort pulse. For ε well below $\varepsilon = 1$, $\langle p_z(\phi_p) \rangle$ features a pronounced minimum as discussed in the main text (Fig. S1). However, as $\varepsilon \rightarrow 1$ (circular polarization) the minimum becomes rapidly shallow and eventually turns into a shallow maximum determined by the pulse envelope.

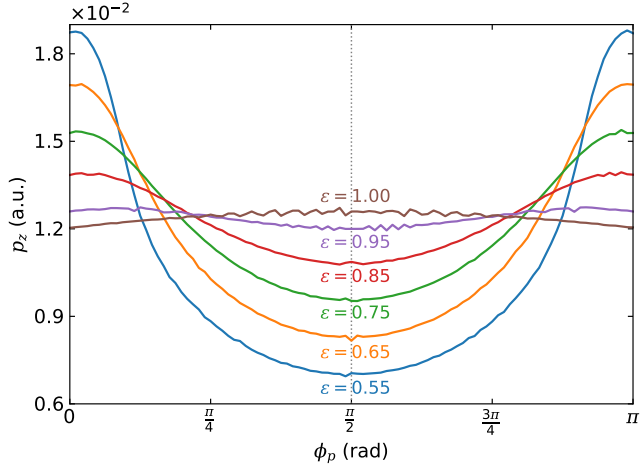


FIG. S1. $\langle p_z(\phi_p) \rangle$ for varying ellipticity. For circular polarization $\varepsilon = 1$, the minimum in $\langle p_z \rangle$ turns into a shallow maximum reflecting the pulse envelope.

S5. WAVELENGTH SCALING

In order for the nondipole transfer of linear momentum to be detected more easily, performing attoclock experiments with midinfrared laser sources is a promising route. Here, we study the wavelength dependence of the final longitudinal momentum transfer while keeping the intensity fixed, as shown in Fig. S2. Clearly, as the wavelength increases, the nondipole effect gets larger and becomes more obvious [panel (a)]. Plotting the angle-integrated final linear momentum as a function of the wavelength, we find a quadratic increase of $\langle p_z \rangle$ with the wavelength [panel (b)] and the intercept is close to but not identical to $I_p/3c$, consistent with Eq. (5) of the main text.

The ionization probability peaks near but not exactly at the minimum of the linear momentum transfer, therefore

$$\langle p_z \rangle \gtrsim \frac{I_p}{3c} + \frac{\epsilon^2 A_0^2}{2c} = \frac{I_p}{3c} + \frac{\epsilon^2 F_0^2}{8\pi^2 c^3} \lambda^2. \quad (\text{S36})$$

As a result, the slope is slightly larger than $\epsilon^2 F_0^2 / 8\pi^2 c^3$, which is confirmed by our results.

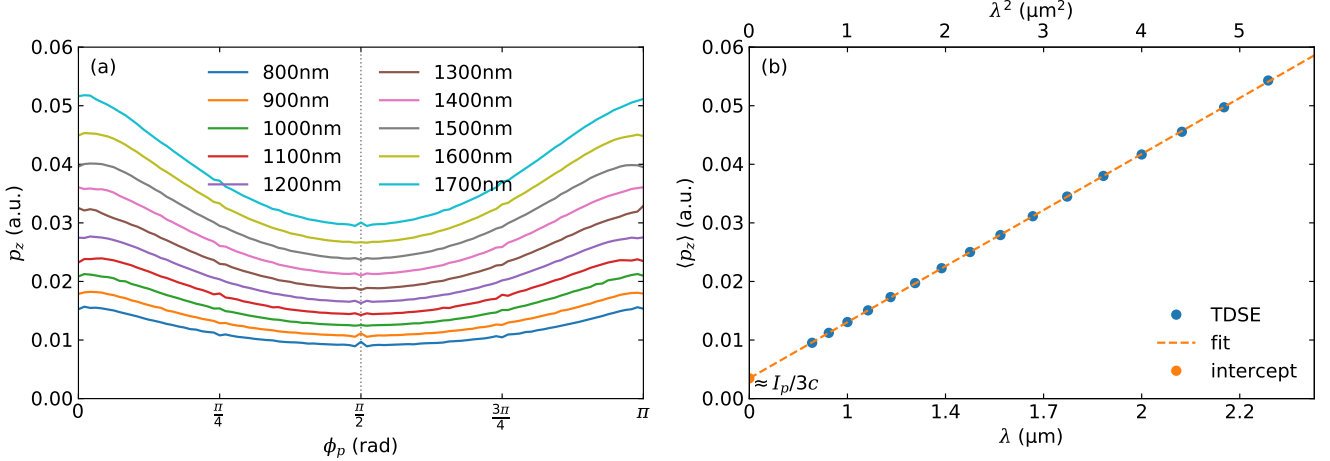


FIG. S2. Final longitudinal momentum for different laser wavelengths in (a) angle-resolved and (b) angle-integrated manner for $\phi_{\text{CEP}} = 0$.

- [1] H. Ni, U. Saalmann, and J. M. Rost, *Phys. Rev. Lett.* **117**, 023002 (2016).
- [2] H. Ni, U. Saalmann, and J. M. Rost, *Phys. Rev. A* **97**, 013426 (2018).
- [3] H. Ni, N. Eicke, C. Ruiz, J. Cai, F. Oppermann, N. I. Shvetsov-Shilovski, and L. W. Pi, *Phys. Rev. A* **98**, 013411 (2018).
- [4] A. D. Bandrauk and H. Shen, *J. Chem. Phys.* **99**, 1185 (1993).
- [5] X. M. Tong and S.-I. Chu, *Chem. Phys.* **217**, 119 (1997).
- [6] X. M. Tong, *J. Phys. B* **50**, 144004 (2017).
- [7] X. Gao, and X. M. Tong, *Phys. Rev. A* **100**, 063424 (2019).
- [8] X. M. Tong, K. Hino, and N. Toshima, *Phys. Rev. A* **74**, 031405(R) (2006).
- [9] G. F. Gribakin and M. Y. Kuchiev, *Phys. Rev. A* **55**, 3760 (1997).
- [10] T. K. Kjeldsen and L. B. Madsen, *Phys. Rev. A* **74**, 023407 (2006).
- [11] D. B. Milošević, G. G. Paulus, D. Bauer, and W. Becker, *J. Phys. B* **39**, R203 (2006).
- [12] N. J. Kylstra, R. M. Potvliege, and C. J. Joachain, *J. Phys. B* **34**, L55 (2001).
- [13] S. P. Goreslavski and S. V. Popruzhenko, *Sov. Phys. JETP* **83**, 661 (1996).
- [14] N. I. Shvetsov-Shilovski, S. V. Popruzhenko, and S. P. Goreslavski, *Laser Phys.* **13**, 1054 (2003).
- [15] S. P. Goreslavski, G. G. Paulus, S. V. Popruzhenko, and N. I. Shvetsov-Shilovski, *Phys. Rev. Lett.* **93**, 233002 (2004).
- [16] M. V. Frolov, N. L. Manakov, A. A. Minina, S. V. Popruzhenko, and A. F. Starace, *Phys. Rev. A* **96**, 023406 (2017).
- [17] A. M. Perelomov, V. S. Popov, and M. V. Terent'ev, *Sov. Phys. JETP* **23**, 924 (1966).
- [18] A. M. Perelomov, V. S. Popov, and M. V. Terent'ev, *Sov. Phys. JETP* **24**, 207 (1967).
- [19] A. M. Perelomov and V. S. Popov, *Sov. Phys. JETP* **25**, 336 (1967).
- [20] V. D. Mur, S. V. Popruzhenko, and V. S. Popov, *J. Exp. Theor. Phys.* **92**, 777 (2001).
- [21] V. S. Popov, *Phys. Usp.* **47**, 855 (2004).
- [22] S. V. Popruzhenko, *J. Phys. B* **47**, 204001 (2014).
- [23] B. M. Karnakov, V. D. Mur, S. V. Popruzhenko, and V. S. Popov, *Phys. Usp.* **58**, 3 (2015).